Enhanced stress and changes to regional seismicity due to the 2015 Mw 7.8 Gorkha, Nepal, earthquake on the neighbouring segments of the Main Himalayan Thrust

Chung-Han Chan [a], Yu Wang [a,*], Rafael Almeida [a], R.B.S. Yadav [b]

[a] Earth Observatory of Singapore, Nanyang Technological University, Singapore
[b] Department of Geophysics, Kurukshetra University, Kurukshetra, India

ABSTRACT

In this study we evaluate stress evolution and change in seismic hazard after the 2015 Gorkha earthquake sequence. We take a methodology usually used in areas with well-established seismic monitoring and apply it to an area with a sparse dataset and a limited time observation window. Our goal is to validate this approach as a rapid response tool for seismic forecasting after large earthquakes. We propose a long-term seismic forecasting model of the Main Himalayan Thrust using the historical earthquake catalogue and regional paleo-seismicity. Through application of the rate-and-state friction model, we evaluate short-term rate evolution after the Gorkha earthquake. The long elapsed time since the last megathrust event and the mainshock coseismic stress increase on the Main Himalayan Thrust suggest high seismic potential in the Lalitpur and Lamjung areas along the fault system. We also calculate the stress change on optimally oriented planes in the region and model the regional seismicity rate using a smoothing kernel method and seismicity since 1921. The location of the consequent earthquakes coincides with areas of high background seismicity rate and areas where stress was enhanced by the Mw 7.8 mainshock and Mw 7.3 aftershock. We model the change of seismic rate over time and project a fast decrease, due to the short aftershock duration assumption we use.

© 2016 The Authors. Published by Elsevier Ltd. This is an open access article under the CC BY-NC-ND license (http://creativecommons.org/licenses/by-nc-nd/4.0/).

1. Introduction

The Mw 7.8 Gorkha, Nepal, earthquake initiated roughly 80 km northeast of Kathmandu (Fig. 1a) on April 25th, 2015, and caused heavy casualties and damages, especially in the Kathmandu and Sindhupalchok areas. Slip models obtained from the Global Seismographic Network (GSN) broadband data suggest that the rupture propagated eastward from its epicentre along the Main Himalayan Thrust (MHT), with rupture dimensions of 150 km along strike by 100 km along dip (Avouac et al., 2015). The National Earthquake Information System (NEIC) of the United States Geological Survey (USGS) reported more than 180 aftershocks within one month of the mainshock. A large amount of aftershocks overlap in map view with the estimated mainshock rupture patch (Fig. 1).

The gently north-dipping MHT is considered the basal detachment of the Himalayan fold and thrust belt (Ni and Barazangi, 1984; Seeber and Armbruster, 1981). The 3 principal thrusts in this orogenic system are, from north to south and older to younger, the Main Central Thrust, the Main Boundary Thrust and the Main Frontal Thrust (MFT) (Gansser, 1964) (inset of Fig. 1), which ramp-up from the MHT. Over the Holocene the MFT has accommodated almost all of the convergence between India and Asia that is taken up across the Himalayas, ~20 mm per year (Ader et al., 2012; Lavé and Avouac, 2000), and is thought to be the only thrust system that is currently active (Lavé and Avouac, 2000).

A question that emerged immediately after this earthquake was how this event would impact the regional seismicity. The elevated seismic activity after the Gorkha mainshock might further contribute to damage buildings and infrastructure. For decades, researchers have used well-located aftershocks from local seismic networks, and high-resolution fault slip models to discuss the change of regional seismicity, and "retro-forecast" the impact to the subsequent events (Chan et al., 2010, 2012b). However, these types of high-quality datasets are not available in many countries, including Nepal. These data also require longer time to collect and process after a major seismic event. Both of these factors limit their use for rapid-response earthquake forecasting models in areas where high-quality data are sparse.

---

* Corresponding author.
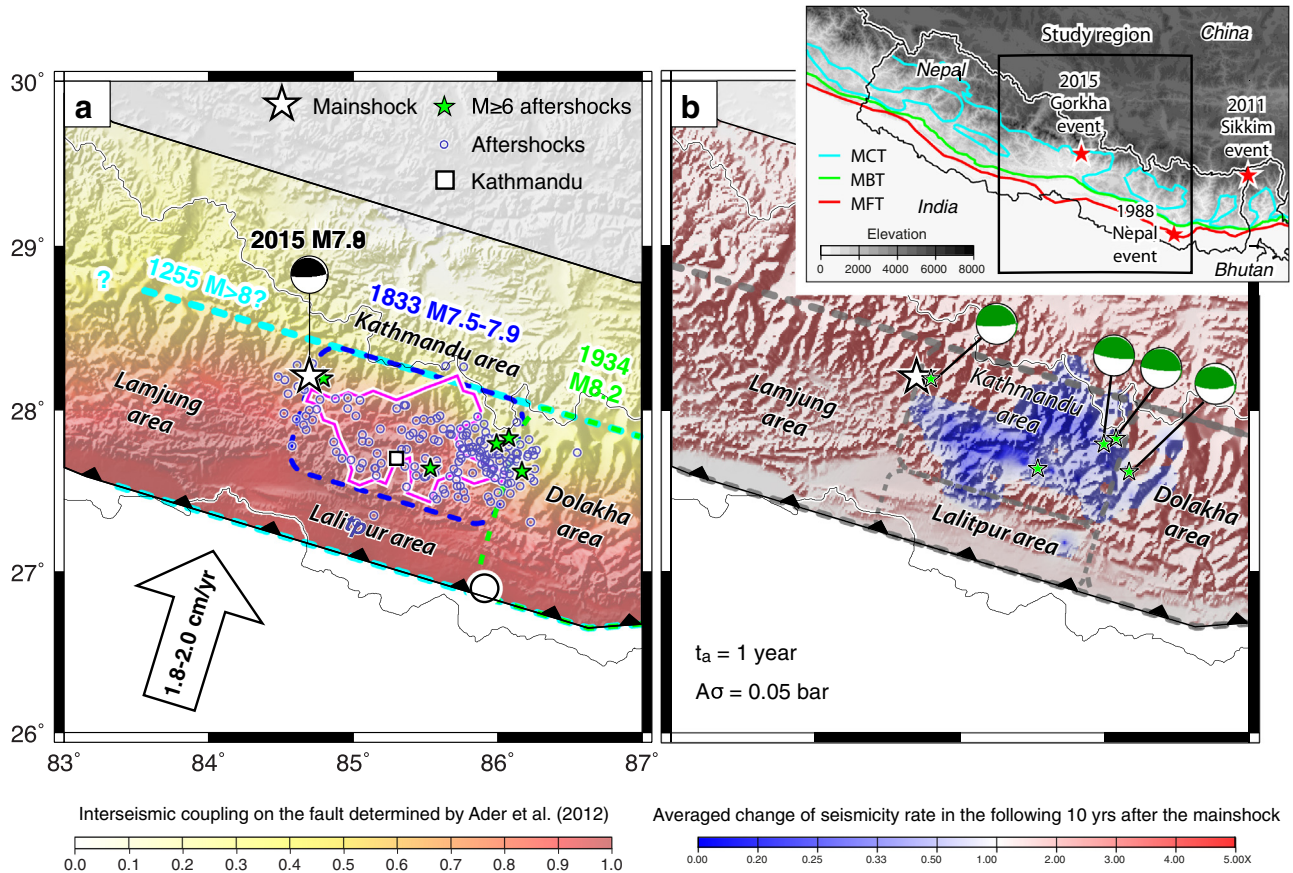 *E-mail address:* y.wang@ntu.edu.sg (Y. Wang).

Fig. 1. (a) Spatial distribution of the interseismic coupling along the MHT, slip patches of historical earthquakes on the megathrust (Bollinger et al., 2014; Mugnier et al., 2013; Sapkota et al., 2013), and distribution of the 2015 sequence. The localities of the MFT investigated by Bollinger et al. (2014) are denoted with a white circle. The magenta contour illustrates the coseismic slip patch of the Gorkha earthquake. The green, blue, cyan dashed contours are the possible rupture regions of the 1934, 1833, and 1255 earthquakes, respectively. (b) Seismicity rate change on the megathrust in the following 10 years after the 2015 Gorkha earthquake. The MHT geometry is defined by Ader et al. (2012). The inset shows the location of the Main Central Thrust (MCT), the Main Boundary Thrust (MBT) and the Main Frontal Thrust (MFT) in cyan, green, and red, respectively, and the red stars show the locations of the 1988 Nepal, 2011 Sikkim and 2015 Gorkha earthquakes. (For interpretation of the references to colour in this figure legend, the reader is referred to the web version of this article.)

In this study we show that this method can be used as a rapid-response tool by developing a forecasting model for both large and moderate earthquakes using datasets that are quickly available after the mainshock. Thus we will work with the seismic catalogue one month after the earthquake. We would like to note that our calculations can be updated in the future when a better earthquake catalogue is available. In this study, we attempt to forecast the probabilities of both megathrust-rupture events on the MHT and subsequent seismicity near the Gorkha rupture area with respect to Coulomb stress change (ΔCFS) imparted by the mainshock. We test our results by comparing the ΔCFS model with the distribution of the aftershocks that occurred within the first month after the mainshock. By using information from published paleoseismological analyses, as well as global and regional earthquake catalogues, we then quantify temporal evolution of the seismicity rate through the application of the rate-and-state friction model of Dieterich (1994).

2. Coulomb stress change and consequent earthquakes on the Main Himalayan Thrust

The ΔCFS calculation followed the constant apparent friction law (Harris, 1998), expressed as:

$$\Delta CFS = \Delta \tau + \mu' \Delta \sigma_n, \tag{1}$$

where $\Delta \tau$ is the shear stress change along the slip direction, μ' is the apparent friction coefficient and $\Delta \sigma_n$ is the normal stress change on

the assumed planes. Generally μ' values lie between 0.2 and 0.8. We tested these μ' end members and concluded that the calculated Coulomb stress changes in both cases were indistinguishable from each other. We used $\mu' = 0.2$, a value inferred from the low deviatoric stress suggested by previous studies (Bollinger et al., 2004; Cattin and Avouac, 2000). We then computed the ΔCFS caused by slip dislocation patches in a homogeneous half-space using the COULOMB 3.3 code (Toda et al., 2011).

To calculate the coseismic ΔCFS, we implemented the slip dislocation model from Avouac et al. (2015). This slip model, together with other earlier coseismic slip models, such as the slip model of the NEIC (http://earthquake.usgs.gov/earthquakes/eventpage/us20002926#scientific_finitefault), shows that no coseismic slip took place on the shallow part (depth < 8 km) of the MHT. This is consistent with the interferometric synthetic aperture radar images from the European Space Agency's Copernicus Sentinel-1A satellite analysed by the Advanced Rapid Imaging and Analysis Center for Natural Hazards (http://aria.jpl.nasa.gov/node/43) and from ALOS-2 data (Lindsey et al., 2015). We evaluated ΔCFS on the MHT using the geometry defined by Ader et al. (2012), a plane with a strike of 287° and a dip of 10°. This geometry is similar to that defined by the focal mechanisms of the mainshock and large aftershocks (Fig. 1b), which have strikes of 295–310° and dips of 7–11° (Global Centroid Moment Tensor, GCMT, and NEIC catalogues) (Ekström et al., 2012). The result can be seen in Fig. 2a. The small discrepancy between the slip patch and the area of coseismic stress drop is due to the difference between the receiver

fault geometry used in our model (Ader et al., 2012) and that of the slip patch modelled using teleseismic data (Avouac et al., 2015).

In addition to the ΔCFS from the M_w 7.8 mainshock, stress changes due to major aftershocks can also control the behaviour of the following earthquakes. Thus, we further evaluated the stress change imparted by the May 12, 2015 M_w 7.3 aftershock using the NEIC slip model (http://earthquake.usgs.gov/earthquakes/event-page/us20002ejl#scientific_finitefault). Our model suggests that the changes in the stress field that occurred due to this aftershock are restricted to the northeast of the mainshock slip patch (Fig. 2b).

3. Possibility of megathrust event in the future

Paleoseismological and historical earthquake studies suggest that the MHT produces megathrust earthquakes with fault ruptures at the surface (e.g., 1255 and 1934 earthquakes) (Sapkota et al., 2013) every several hundred years, as well as other destructive events (e.g., 1833) that are likely blind and do not leave significant evidence in the geological record (Avouac, 2007). Based on historical records, at least three megathrust events have struck central Nepal in the past 750 years (i.e., in 1255, 1833, 1934) (Fig. 1a) (Bollinger et al., 2014). The 1934 event, $M \sim 8.2$–8.4 (Chen and Molnar, 1977; Singh and Gupta, 1980), ruptured the Dolakha area, east of Kathmandu (Fig. 1). The shaking records of the 1833 earthquake (Bilham, 1995) suggest that this 19th century event had a rupture area similar to that of the 2015 Gorkha earthquake. The rupture of the destructive 1255 earthquake is comparable to or even longer than the 1934 earthquake, from Dolakha to Lamjung area, though the rupture length for this earthquake is not well constrained (Bollinger et al., 2014). These large earthquakes emphasize the importance of understanding the seismic hazard in central Nepal from the MHT.

Bollinger et al. (2014) documented the rupture history of two strands of the MFT in an area southeast of Kathmandu using a combination of terrace elevation surveying, terrace dating and trenching (Fig. 1a). A flight of 5–7 strath terraces, interpreted to be tectonically uplifted, was studied. These terraces span a time of 3.6–4.5 kyrs. Based on their results Bollinger et al. (2014) suggest that the average return periods of the great surface-breaking Himalayan earthquakes ($M_w \geqslant 8.0$ events on the MHT such as the 1255 and 1934 events) in the Dolakha area range between 750 ± 140 and 870 ± 350 years, depending on the interpretation of the preserved sedimentary record. These recurrence intervals assume a characteristic earthquake model. Even though studies suggest that this model may not be applicable in all tectonic settings (Goldfinger et al., 2012; Weldon et al., 2004), at present these are the best estimates available for central Nepal. Based on this, qualitatively, we can expect that the probability of surface-rupturing megathrust event in Dolakha region might be low in the coming near future, as the most recent rupture took place in 1934. In contrast, the shallow portion of MHT beneath both the Lalitpur and the Lamjung areas possibly has not ruptured since 1255, suggesting a higher earthquake probability in the coming future.

To quantitatively evaluate the long-term seismicity rate of the large megathrust earthquakes, we implemented the Brownian Passage Time (BPT) model (Ellsworth et al., 1999) to express the earthquake probability density function (*PDF*) as:

$$PDF = \left(\frac{\mu}{2\pi\alpha^2 t^3}\right)^{1/2} \exp\left(-\frac{(t-\mu)^2}{2\alpha^2 \mu t}\right), \tag{2}$$

where μ is the mean recurrence interval (taken from paleoseismological studies), t is the elapsed time since the last event and α is the aperiodicity. We assumed that the aperiodicity is the ratio of standard deviation to mean recurrence interval. To further quantify the

earthquake probability, we follow the procedure of Erdik et al. (2004) and assume:

$$P(t, \Delta t) = \frac{\int_t^{t+\Delta t} f(t) dt}{\int_t^{\infty} f(t) dt}, \tag{3}$$

where $P(t, \Delta t)$ is the earthquake probability within the next Δt years, assuming that no earthquake has occurred in the past t years; $f(t)$ is the seismicity density function, presented by the BPT model in Eq. (2). Considering t as the elapsed time since the last MFT-rupturing event (in 1255) on the Lalitpur and Lamjung area and aperiodicity values between 0.3 and 0.7, the probability of a rupture in the next decade (i.e. $\Delta t = 10$ years) is between 1.7% (recurrence interval of 870 years; aperiodicity value of 0.7) and 4.1% (recurrence interval of 750; aperiodicity value of 0.3). The probabilities become larger when a longer period of time is considered. For example, the calculated earthquake probabilities are between 8.4% and 19.3% in the coming 50 years (i.e. $\Delta t = 50$ years).

Stress changes after a large earthquake alter seismicity behaviour in a short-term period, which can be illustrated by the rate-and-state friction model (Dieterich, 1994). We will quantify this seismicity change and evaluate its effect to better constrain the probability of a megathrust earthquake. Based on the procedure proposed by (Chan et al., 2010), the evolution of the seismicity rate change $\Delta R(M, x, t)$, considering ΔCFS by the n'th event $\Delta CFS_n(x)$ at the site of interest x as a function of magnitude, M, and time, t, is presented as follows:

$$\Delta R(M, x, t) = \frac{1}{\left[\frac{1}{\Delta R_{n-1}(M,x)} \exp\left(\frac{\Delta CFS_n(x)}{A\sigma}\right) - 1\right] \exp\left(-\frac{t-t_n}{t_{na}}\right) + 1}, \tag{4}$$

where $\Delta R_{n-1}(M, x)$ is the seismicity rate change promptly before the n'th event based on the rate evolution by previous events (i.e. $\Delta R_0(M, x)$); $A\sigma$ is a constitutive parameter of the model; t_n is the occurrence time of the n'th source event and t_{na} is the aftershock duration. The aftershock duration t_{na} is related to $A\sigma$ through

$$t_{na} = \frac{A\sigma}{\dot{\tau}}, \tag{5}$$

where $\dot{\tau}$ is the fault/regional stressing rate (Dieterich, 1994). To obtain the regional aftershock duration, we examined the time series of the 1988 Nepal (M_w 6.8) and 2011 Sikkim (M_w 6.9) sequences.

To model the temporal decay of seismicity rate, $n(t)$, we considered the modified Omori's Law of Utsu (1961), which can be denoted as follows:

$$n(t) = \frac{t}{(c+t)^p} \tag{6}$$

where k, c, and p are constants that represent the number of observed earthquakes, the rate of decay and the delay of the decay, respectively. In this study, we assumed $c = 0$, suggesting no time delay for the decay. k- and p-values for each sequence were obtained using a least square fit with the temporal distribution of subsequent seismicity after the mainshock. We obtained aftershock durations of 0.99 and 1.77 years for the 1988 Nepal and 2011 Sikkim sequences, respectively (Fig. 3a and b). Thus, we fix the aftershock duration to 1 year for the application of the rate-and-state friction model. Similar short aftershock periods have been observed at other tectonically active regions with high fault slip rate, including fault systems in California and Taiwan (e.g., Chan and Wu, 2012; Dieterich, 1994). To test this assumption, we modelled the temporal distributions of the 2015 Gorkha sequence through the modified Omori's Law (Utsu, 1961) using the earthquake parameters obtained from the NEIC catalogue (Fig. 3c). The result suggests the aftershock period of this sequence is 2.08 year, close to our assumption (1 year). The large deviation of the decay model in the Gorkha case (Fig. 3c) can be attributed to the short observation period (one
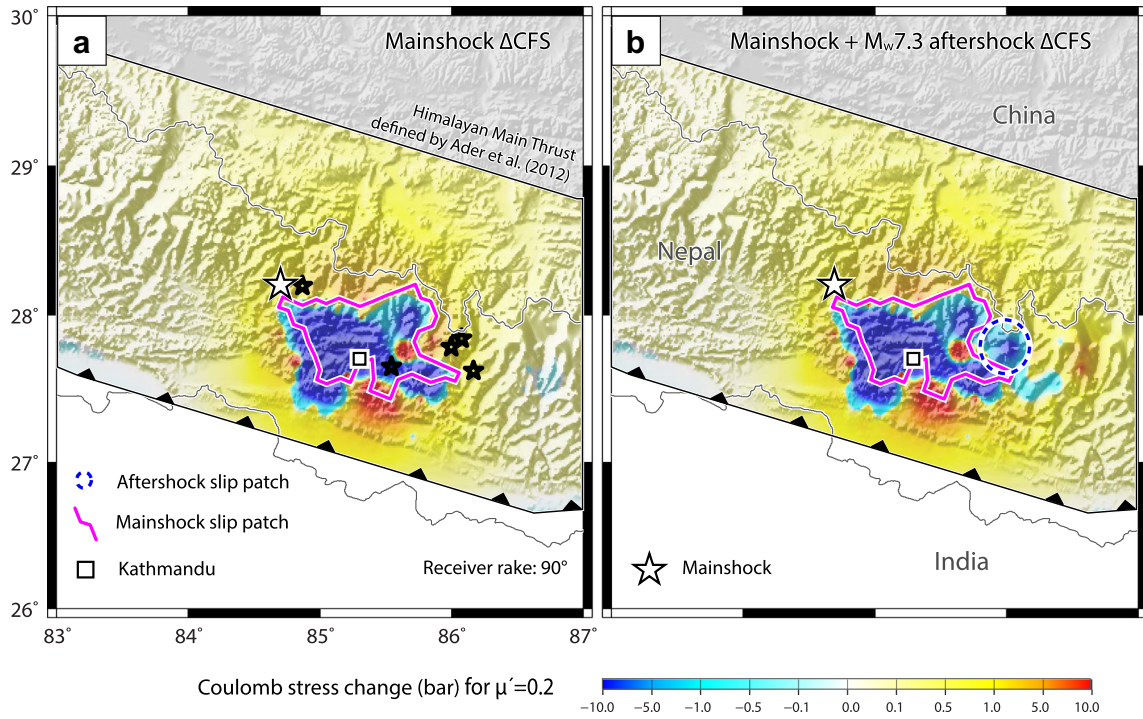
Fig. 2. The Coulomb stress change (ΔCFS) on the MHT imparted by (a) the M7.8 Gorkha earthquake, and (b) both the mainshock and the M7.3 aftershock. The magenta contour illustrates the coseismic slip patch of the Gorkha earthquake. The blue dashed contour in (b) illustrates the rupture patch of the M7.3 aftershock. (For interpretation of the references to colour in this figure legend, the reader is referred to the web version of this article.)
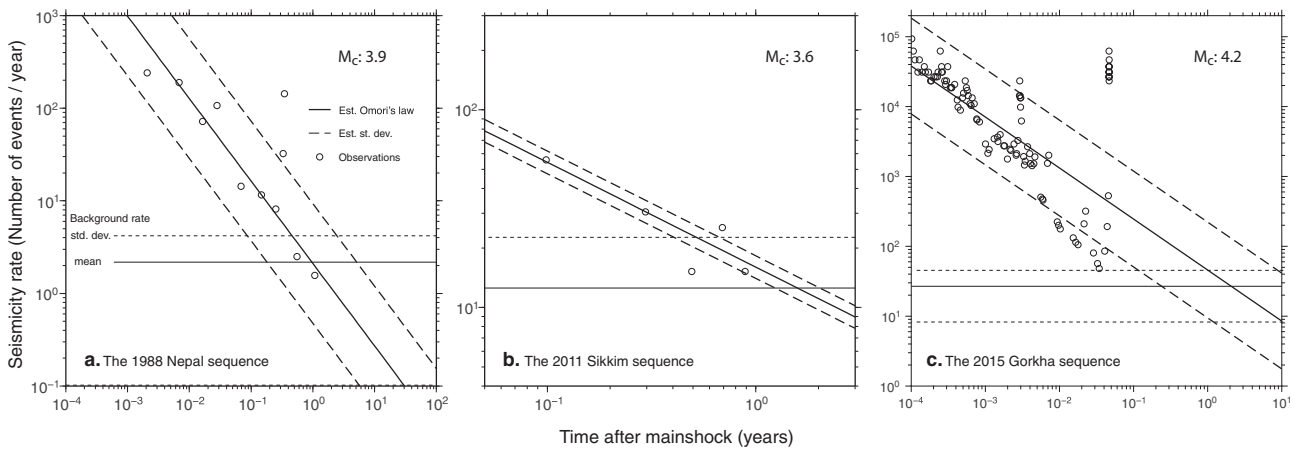

Fig. 3. The observed and modelled temporal distributions of (a) the 1988 Nepal, (b) 2011 Sikkim and (c) 2015 Gorkha sequences. Models were done using the modified Omori law of Utsu (1961). Seismicity rates drop back to background level in 0.99, 1.77 and 2.08 years, respectively. Mc denotes the magnitude of completeness available for each earthquake, based on the lease-square regression result of each earthquake sequence.

month after the mainshock) and sparse events due to the high magnitude of completeness of the used catalogue (M_c 4.2).

Based on the observation of seasonal correlation between seismicity and stress rate, Bettinelli et al. (2008) suggested a small $A\sigma$ of <0.08 bars for Nepal. Based on this we assumed a fixed value of 0.05 bar for our calculations. The assumptions mentioned above imply a stressing rate of 0.05 bar/year according to Eq. (5), consistent with the stressing rate of 0–0.1 bar/year deduced from the MHT coupling model in Ader et al. (2012). Using these parameters, we implemented the rate-and-state friction model to evaluate seismicity rate change (Fig. 1b). The stress perturbation by the Gorkha earthquake and its M_w 7.3 aftershock (Fig. 2) results in a seismicity rate decrease in the rupture patches on the MHT whereas the rate

increases in the peripheral regions. Our estimation suggests that the average seismicity rates on the MHT in the Lamjung, Lalitpur, and Dolakha area could be elevated as much as 4.0, 4.8, and 4.8 times, respectively, in the following 10 years, compared to the rate before the mainshock.

Using these new average seismicity rates we can re-calculate the probabilities of a megathrust earthquake. To do this using Eq. (3), we obtained the seismicity density function by multiplying seismicity rates from the BPT model (Eq. (2)) and the rate-and-state friction model (Eq. (4)). Based on this, the probability of an earthquake occurring on the MHT in the next decade is 24% and 11% for mean recurrence intervals of 750 ± 140 and 870 ± 350 years, respectively. These probabilities are considerably higher than the initially

calculated ones (6.3% and 2.4%) highlighting the enhanced seismic hazard of the region after the Gorkha earthquake.

4. Coseismic Coulomb stress change on optimally oriented planes and consequent earthquakes in the region

In the previous sections, we have generated a model to forecast the probability of the next megathrust events along the MHT. Besides the MHT, other secondary faults may generate moderate-to-large earthquakes that could result in disasters as well (e.g., the 1988 M_w 6.8 Nepal and 2011 M_w 6.9 Sikkim earthquakes). These secondary faults may not have a similar fault geometry to the MHT (e.g., de la Torre et al., 2007), thus, to assess the regional earthquake potential of these structures requires a different model.

The aftershock distribution after the Gorkha earthquake was asymmetric, with more aftershocks located to the east of the main-shock rupture patch. This is consistent with dynamic stress trigger-ing having some influence in their distribution, though we do not have the strong motion data necessary to quantify this aspect. Recent studies, however, have shown that static stress changes are central in controlling the clustering of small earthquakes (e.g., Green et al., 2015) and thus, we will focus on this factor in this study. We modelled the coseismic ΔCFS on optimally oriented planes (OOPs) (King et al., 1994), as the geological and the seismological data do not provide adequate information to predetermine the ori-entation of these secondary receiver faults near the rupture patch.

OOP determination requires knowledge of not only the ΔCFS of an earthquake, but also regional stress orientation and deviatoric stress. We used the GCMT mainshock focal mechanism (Fig. 1a) to infer the regional stress orientation and assumed a low devia-toric stress of 100 bars for the regional stress state based on the stress estimation from Bollinger et al. (2004). Due to insignificant coseismic stress change away from the rupture patch, the OOPs outside the coseismic slip patch keep the mechanism imposed by the regional stress (shallow thrust). In contrast, the orientations of OOPs are diverse close to the rupture zone due to comparable stress magnitudes of the regional stress and the coseismic ΔCFS (inset in Fig. 4d).

We evaluated the ΔCFS resolved on the stress-defined OOPs. We first evaluate the ΔCFS at depths of 10, 15 and 20 km, on a 2 km × 2 km grid map (Fig. 4a–c). The model shows that a signifi-cant stress increase patch migrates toward to northeast with depth, which corresponds to the dipping of the rupture patch. In the vicinity of the rupture patch, however, the stress dropped dur-ing the coseismic period. This model does not fully forecast the aftershock distribution (blue[1] circles in Fig. 4a–c) as some of them are located in the stress shadow zone, however this observation depends on adequate depth control for the aftershocks, which is not available for the vast majority of them. The failure of this model may also be due to uncertainty of the resolution of the finite rupture model, e.g. aftershocks may take place on strong, unruptured small patches too small to be resolved (Chan et al., 2012b). In order to improve the forecasting quality, we followed the procedure of Catalli and Chan (2012) and evaluated ΔCFS at different depths at each calculation grid node and reported the maximum one (Fig. 4d). The resulting map shows the maximum stress value for depths of 10–20 km at each node. This model shows significant stress increase overlapping in map view with the slip patch, where a large amount of aftershocks took place. The better forecasting ability for this model can be attributed to minimization of the effect of hypocentral depth uncertainties and of rupture geometry (Catalli and Chan, 2012).

To validate our results statistically, we compared ΔCFS models with the spatial distribution of the aftershocks using the Molchan diagram (Molchan, 1990, 1991), which was designed for evaluating forecasting ability. We present the "fraction occupied by alarm" as the proportion of the study area having a ΔCFS equal to or higher than a threshold, defined as "alarm". The "ratio of failure to pre-dict" indicates the proportion of aftershocks that locate in a region with a lower ΔCFS than the alarm. In other words, when data points are distributed along the diagonal line, the distribution of aftershocks is uniform and independent of the ΔCFS. A convexity suggests that the majority of the aftershocks occurred within regions with negative ΔCFS as compared to the entire area and a concavity suggests that the majority of the aftershocks occurred in an area with positive ΔCFS. Based on the results of the Molchan diagram, the forecasting ability of the ΔCFS model using individual target depths is marginal (green dots in Fig. 5a) since only 63% of the aftershocks locate in stress increase zone (Fig. 4a–c). On the contrary, the maximum ΔCFS model shows a convexity distribu-tion in the diagram (red dots in Fig. 5a), which suggests that as the maximum ΔCFS model has a larger area of stress increase stress, aftershocks tend to occur in the region with highest stress increase (Fig. 4d).

The agreement of positive stress changes on OOPs and the area with dense aftershocks was also observed during the 1999 Chi–Chi earthquake sequence in Taiwan. There it was shown that the focal mechanisms of the modelled OOPs and the observed aftershocks were similar (Chan et al., 2012a). We emphasize that our model implies that most small subsequent earthquakes likely take place on secondary faults above and below the MHT, rather than on the MHT itself.

5. Seismicity rate forecasting model

In order to propose a seismicity-forecast model for the study region, we calculated both background regional seismicity rate and regional rate change resulting from the Gorkha earthquake. Previous studies (e.g., Woo, 1996) have determined background rate by summarizing seismic activity during the period with a complete earthquake catalogue, described as follows:

$$\lambda(M, x) = \sum_{i=1}^{N_M} \frac{K(M, x - x_i)}{T_M},$$ (7)

where $\lambda(M, x)$ is the background rate at the site of interest, x, as a function of magnitude, M; $K(M, x - x_i)$ represents a smoothing Ker-nel as a function of magnitude and distance between the site of interest, x, and the i'th earthquake, x_i; T_M represents the period of a complete catalogue with a magnitude threshold; and N_M repre-sents the total number of earthquakes with magnitudes larger than the threshold. We followed the same approach as Woo (1996), that described the Kernel function $K(M, x - x_i)$ as:

$$K(M, x - x_i) = \frac{PL - 1}{\pi H^2(M)} \left(1 + \left(\frac{x - x_i}{H(M)} \right)^2 \right)^{-PL},$$ (8)

where PL is a power law index with recommended values between 1.5 and 2.0, corresponding to a cubic or quadratic decay of seismic activity with hypocentral distance (Molina et al., 2001). Previous studies (Chan et al., 2010, 2012b) concluded that the difference of the results is insignificant when PL is assumed to be in between 1.5 and 2. In this study, we assume $PL = 2.0$. $H(M)$ is the bandwidth function defined as the mean distance of nearest events as a func-tion of magnitude, M, in a catalogue. The function $H(M)$ can be rep-resented as follows:

$$H(M) = c \cdot e^{d \cdot M}$$ (9)

---

[1] For interpretation of colour in Fig. 4, the reader is referred to the web version of this article.
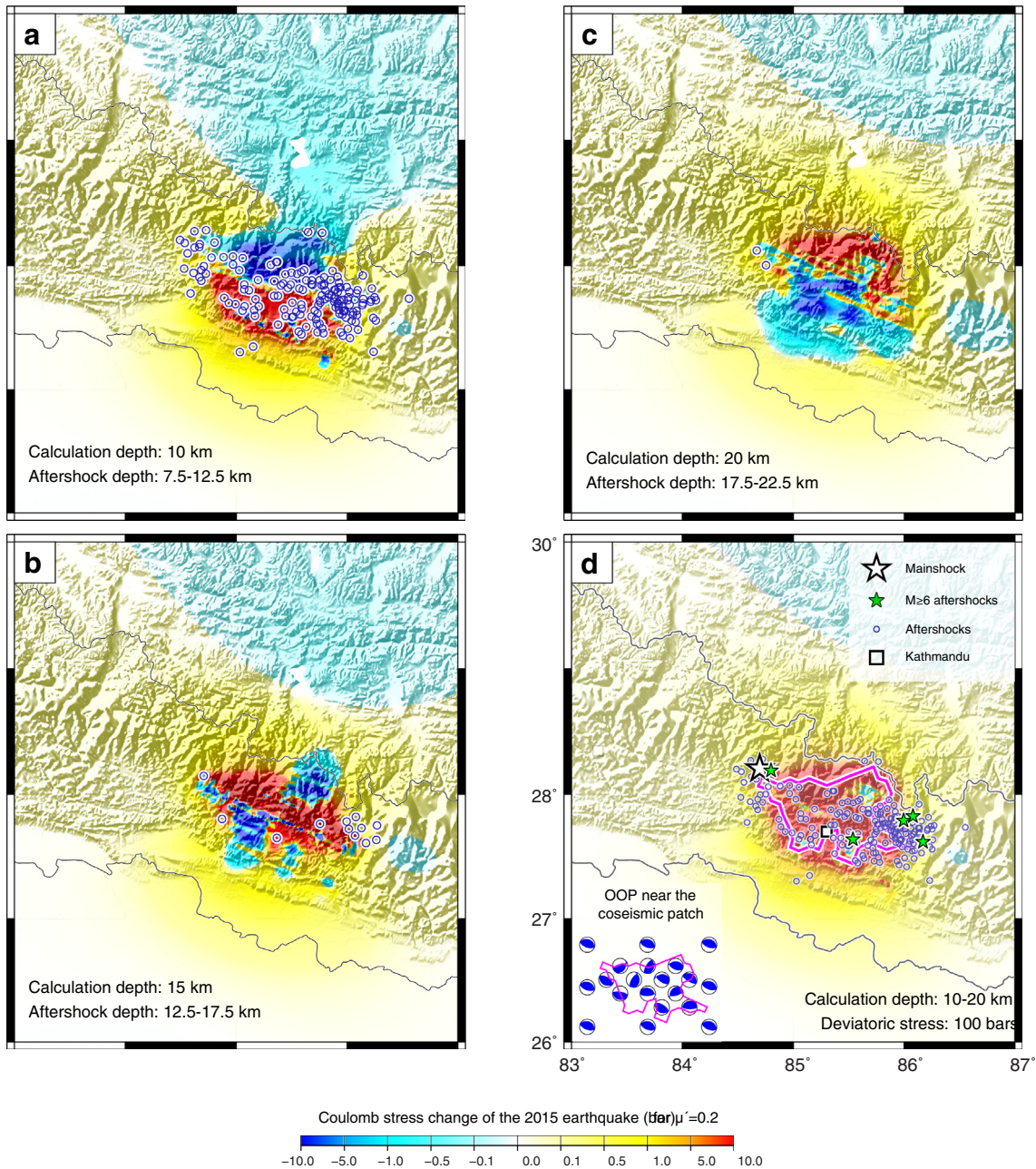
Fig. 4. The coseismic ΔCFS due to Mw 7.8 Gorkha earthquake resolved on the optimally oriented planes (OOP) at depths of (a) 10 km, (b) 15 km, (c) 20 km, and (d) the maximum ΔCFS among the three layers. The distribution of the OOPs near the coseismic slip patch is presented in the inset. Note that the ΔCFS calculation grids are denser than the spacing presented in the inset. The magenta contour illustrates the coseismic slip patch of the Gorkha earthquake.

where c and d are constants that represent the seismicity rate and rate decrease exponentially with magnitude, respectively, obtained from a regression of an earthquake catalogue. This approach forecasts seismicity rate based on the averaged seismic activity during the observation period and minimizes the factor of temporal evolution.

To obtain a background rate, the model requires a complete earthquake catalogue. We implemented the catalogue of Yadav et al. (2009) and updated it to 2015 using the NEIC database. Yadav et al. (2009) integrated earthquake location parameters from the International Seismological Centre (ISC), the NEIC, the GCMT Project, and the seismicity data compiled by Gupta et al. (1986). The various magnitude scales are harmonized to moment magnitude (Mw), with the magnitude of completeness (Mc) about 4.0 since 1987 (Yadav et al., 2009). Since we assume consequent

aftershocks as triggered by the mainshock ΔCFS, aftershocks were excluded from the catalogue using the declustering approach developed by Uhrhammer (1986). Considering the complete part of the catalogue since 1987, we estimated the c- and d-values of the bandwidth function to be 0.27 and 1.01, respectively. These parameters provide the basis to generate the background seismicity rate in the region (Fig. 6). Our seismicity rate map before the 2015 mainshock clearly indicates a high seismicity rate area at the eastern edge of the Gorkha rupture patch that coincides with the dense aftershock zone after the Gorkha earthquake. The other seismicity rate peak located north of the Gyachung Kang (Fig. 6) is possibly associated with the active north-trending normal faults located in the southern Tibetan Plateau (e.g., Armijo et al., 1986; Kapp et al., 2008). This patch, however, shows no increase in seismicity related to the mainshock. The absence of aftershocks at this
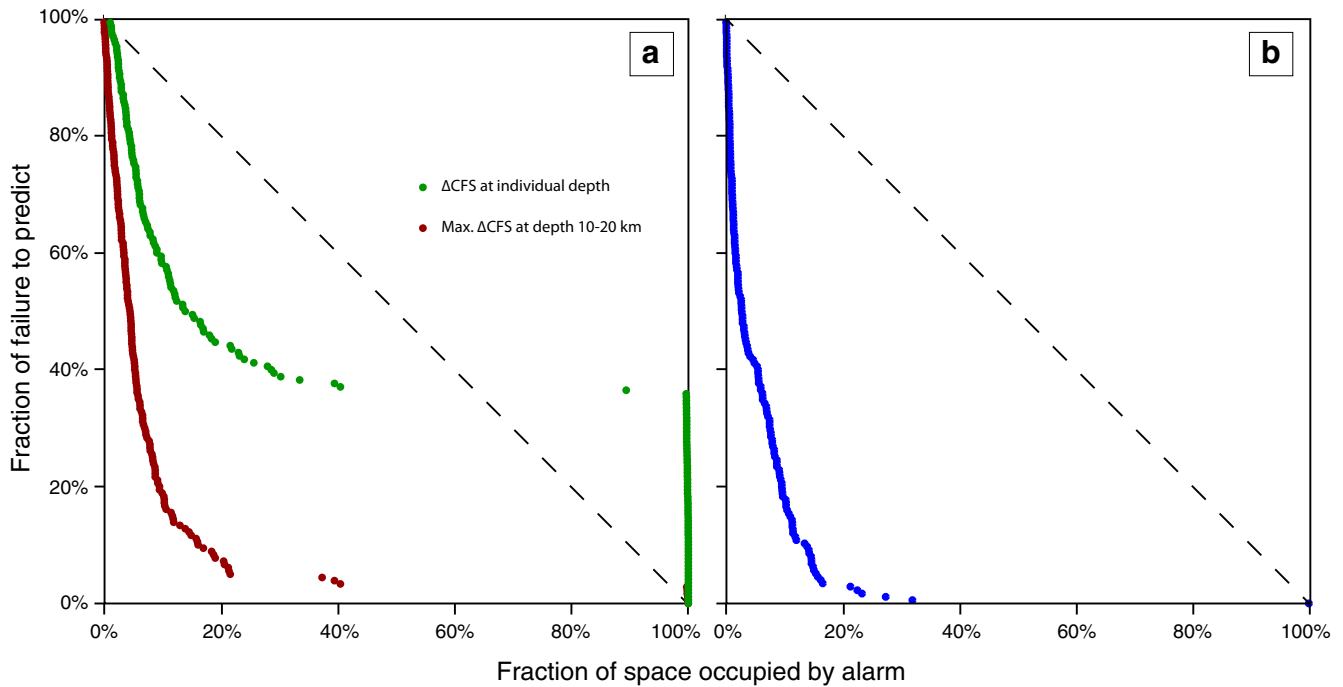
Fig. 5. The Molchan diagram, used for investigating the correlation between forecasting models and spatial distribution of the aftershocks. (a) Green dots represent the combined results for the ΔCFS at depths of 10 km, 15 km, and 20 km and the red dots represent the results using the maximum ΔCFS from the three depths. (b) Blue dots represent the correlation between forecasting models based on background rate and the rate-and-state friction model and spatial distribution of the aftershocks. (For interpretation of the references to colour in this figure legend, the reader is referred to the web version of this article.)

patch supports our Coulomb stress modeling result that only minor stress changes propagated far away from the coseismic slip patch (Fig. 4d).

Fig. 7 shows our forecast of the temporal seismic rate evolution in central Nepal after the Gorkha earthquake. Our forecast suggests a significant rate increase around the mainshock slip patch that correlates well with the aftershock distribution. Although the aftershock rate may decay quickly after the mainshock, our model suggest that the average seismicity rate within the first year post-mainshock is still 2.5 times higher than the background rate (Fig. 7a). Our model also shows that in a decade the average seis-micity rate would be close to, but still 30% higher than, the back-ground rate before the Gorkha earthquake (Fig. 7b). The rapid rate decay is attributed to the assumption of short aftershock dura-tion (one year), consistent with the temporal seismicity decay behaviour after the 2015 Gorkha earthquake (Fig. 3c).

When we compare the aftershock occurrences to the temporal and spatial distributions predicted by the modified Omori Law and the rate-and-state friction model, respectively, we see that 174 out of the 175 (more than 99%) aftershocks were located in the area with forecasted rate higher than 3.32 events per 10 years per 100×100 km^2 (Fig. 7), which corresponds to the highest 32-percentile forecasted rate in our model. To validate the spatial dis-tribution of our forecasting model we again use the Molchan dia-gram (Fig. 5b). This plot shows the excellent correlation between the earthquake distribution prediction and the actual locations.

To quantitatively evaluate the credibility of our forecast model through time, we implemented the N-test (Eqs. (8a) and (8b) in Zechar et al., 2010). This test is based on $\delta_1(t)$ and $\delta_2(t)$, which rep-resent the correlation between numbers of observed and fore-casted events using a right-continuous Poisson cumulative distribution function. A forecast will be accepted only if $\delta_1(t) < 1 - \alpha_{eff}$ and $\delta_2(t) > \alpha_{eff}$, where α_{eff} represents the effective significance value. We followed Zechar et al. (2010) and assumed
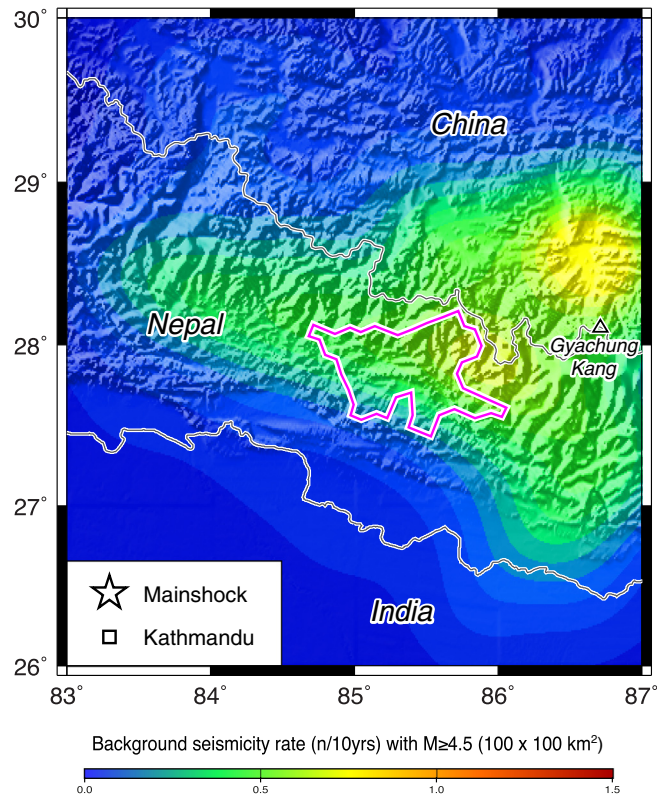

Fig. 6. Spatial distribution of the background seismicity rate calculated from the updated earthquake catalogue of Yadav et al. (2009). The magenta contour illustrates the coseismic slip patch of the Gorkha earthquake.

$\alpha_{eff} = 0.025$. We evaluate $\delta_1(t)$ and $\delta_2(t)$ for the number of $M \geqslant 4.5$ earthquakes in the first month after the Gorkha main-
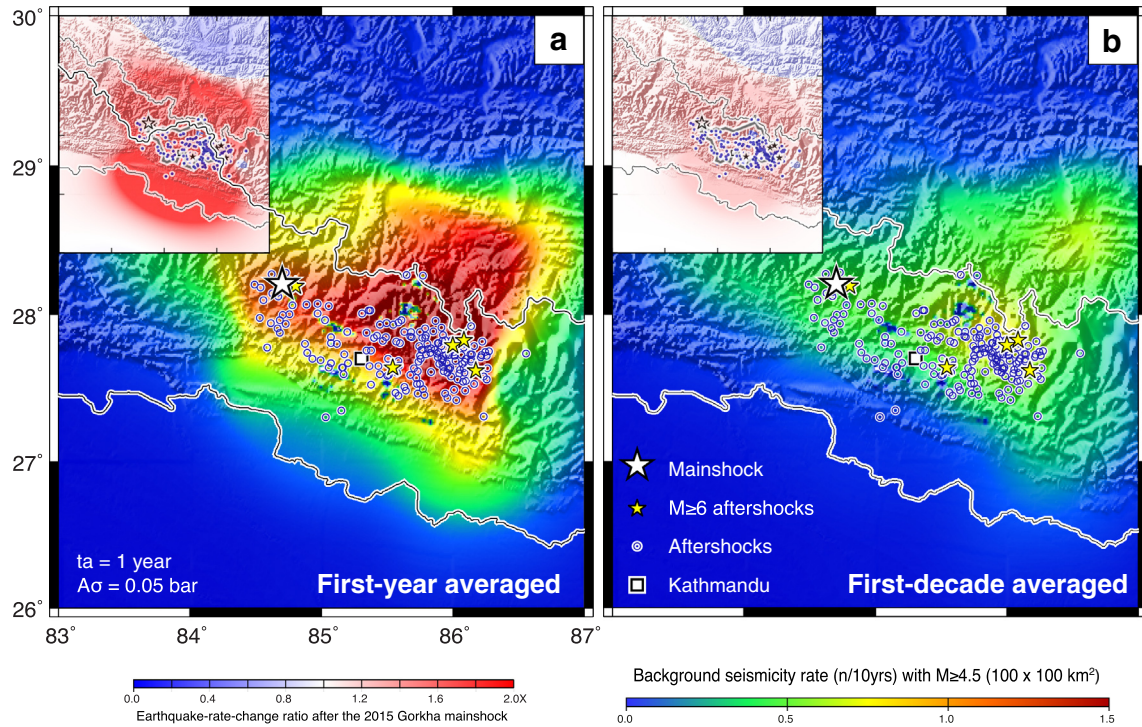
Fig. 7. Averaged regional seismicity rate in (a) 1 year and (b) 10 years post-Gorkha earthquake. Insets present corresponding earthquake-rate-change ratios based on the maximum ΔCFS calculation resolved on the OOP at depths of 10, 15, and 20 km.
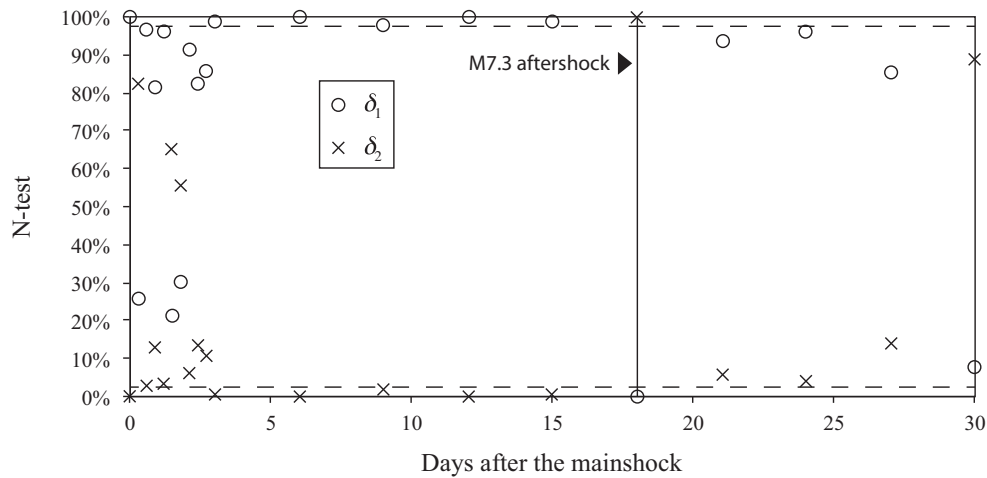

Fig. 8. N-test for evaluating the consistency between the total number of forecasted and observed earthquakes within one month after the mainshock. The dashed lines denote the 2.5% and 97.5% boundary of effective significance value. The solid line denotes the occurrence time of the M7.3 aftershock.

shock (Fig. 8). The test shows our model forecast the number of events well in the first three days. Afterward, our model is less satisfied due to over-prediction in this period (i.e. $\delta_1(t) > 1 - \alpha_{eff}$ and $\delta_2(t) < \alpha_{eff}$). The numbers of observed and forecasted events, again, become comparable after occurrence of the M_w 7.3 aftershock. The change of the N-test result over time suggests that our current model does not perform perfectly in the daily-scaled forecast. However, this model forecast quantitatively well in a monthly scale, including the large aftershock and its secondary aftershocks.

The dissatisfaction of our daily forecast result is likely resulting from the simplification of our proposed forecast model, as this model is based on the Coulomb stress changes related to the M_w 7.8 mainshock and M_w 7.3 aftershock with constant background stressing rate. We are aware of other factors that may control behaviours of consequent earthquakes, e.g., stress change by after-

slip (Chan and Stein, 2009; Perfettini and Avouac, 2007). However, implementation of these factors requires postseismic geodetic observations, which does not fulfill the scope of this study, i.e. proposing a forecasting model quickly after the mainshock.

6. Conclusions

In this study, we evaluated stress evolution following the 2015 Gorkha earthquake sequence and future seismic hazard potential on both the megathrust and the surrounding area, using the data available within one month after the mainshock. We showed that the location of the consequent earthquakes coincides with areas where stress on the optimally oriented planes was enhanced by the M_w 7.8 mainshock and M_w 7.3 aftershock. We reviewed the

historical catalogue and regional paleo-seismicity to propose long-term forecasting for large earthquakes on the Main Himalayan Thrust. Through application of the rate-and-state friction model, we evaluated short-term rate evolution after the Gorkha earthquake. The long elapsed time since the last event and the coseismic stress increase on the Main Himalayan Thrust suggest high seismic potential in the Lalitpur and Lamjung segments of the fault. We also modelled the regional seismicity rate using a smoothing kernel method and seismicity since 1921. A high seismicity rate was observed at the eastern edge of the mainshock rupture, which coincides with an area with large amount of aftershocks. Study of previous aftershock sequences leads us to assume a short aftershock duration, 1 yr, which causes the subsequent seismicity rate to descend dramatically over time in our forecast. We show that this methodology, though commonly used for areas with long monitoring histories, may be used as a rapid-response tool after a large earthquake, which would allow quantifying the short and long term seismic risk. The outcomes of this study determine key parameters for subsequent seismic hazard assessment, a critical component for the short and long term planning of the recovery of the people and infrastructure affected by the Gorkha earthquake sequence.

Acknowledgements

References

Ader, T. et al., 2012. Convergence rate across the Nepal Himalaya and interseismic coupling on the main himalayan thrust: implications for seismic hazard. J. Geophys. Res. 117 (B4). http://dx.doi.org/10.1029/2011jb009071.

Armijo, R., Tapponnier, P., Mercier, J.L., Han, T.L., 1986. Quaternary extension in southern Tibet – field observations and tectonic implications. J. Geophys. Res. 91 (B14), 13803–13872. http://dx.doi.org/10.1029/JB091iB14p13803.

Avouac, J.-P., 2007. Mountain building: from earthquakes to geological deformation. In: Dynamic Processes in Extensional and Compressional Settings: Treatise on Geophysics. Elsevier, Amsterdam, pp. 377–439. http://dx.doi.org/10.1016/B978-044452744-6.00112-7.

Avouac, J.-P., Meng, L., Wei, S., Wang, T., Ampuero, J.-P., 2015. Lower edge of locked Main Himalayan Thrust unzipped by the 2015 Gorkha earthquake. Nat. Geosci. http://dx.doi.org/10.1038/ngeo2518.

Bettinelli, P., Avouac, J.P., Flouzat, M., Bollinger, L., Ramillien, G., Rajaure, S., Sapkota, S., 2008. Seasonal variations of seismicity and geodetic strain in the Himalaya induced by surface hydrology. Earth Planet. Sci. Lett. 266 (3–4), 332–344. http://dx.doi.org/10.1016/j.epsl.2007.11.021.

Bilham, R., 1995. Location and magnitude of the 1833 Nepal earthquake and its relation to the rupture zones of contiguous great himalayan earthquakes. Curr. Sci. 69 (2), 101–128.

Bollinger, L., Avouac, J.P., Cattin, R., Pandey, M.R., 2004. Stress buildup in the Himalaya. J. Geophys. Res. 109 (B11). http://dx.doi.org/10.1029/2003jb002911.

Bollinger, L., Sapkota, S.N., Tapponnier, P., Klinger, Y., Rizza, M., Van der Woerd, J., Tiwari, D.R., Pandey, R., Bitri, A., de Berc, S.B., 2014. Estimating the return times of great Himalayan earthquakes in eastern Nepal: evidence from the Patu and Bardibas strands of the Main Frontal Thrust. J. Geophys. Res. 119 (9), 7123–7163. http://dx.doi.org/10.1002/2014jb010970.

Catalli, F., Chan, C.-H., 2012. New insights into the application of the Coulomb model in real-time. Geophys. J. Int. 188 (2), 583–599. http://dx.doi.org/10.1111/j.1365-246X.2011.05276.x.

Cattin, R., Avouac, J.P., 2000. Modeling mountain building and the seismic cycle in the Himalaya of Nepal. J. Geophys. Res. 105 (B6), 13389–13407. http://dx.doi.org/10.1029/2000jb900032.

Chan, C.-H., Hsu, Y.-J., Wu, Y.-M., 2012a. Possible stress states adjacent to the rupture zone of the 1999 Chi-Chi, Taiwan, earthquake. Tectonophysics 541–543, 81–88. http://dx.doi.org/10.1016/j.tecto.2012.03.031.

Chan, C.-H., Sørensen, M.B., Stromeyer, D., Grünthal, G., Heidbach, O., Hakimhashemi, A., Catalli, F., 2010. Forecasting Italian seismicity through a spatio-temporal physical model: importance of considering time-dependency and reliability of the forecast. Ann. Geophys. 53 (3), 129–140. http://dx.doi.org/10.4401/ag-4761.

Chan, C.-H., Stein, R.S., 2009. Stress evolution following the 1999 Chi-Chi, Taiwan, earthquake: consequences for afterslip, relaxation, aftershocks and departures from Omori decay. Geophys. J. Int. 177 (1), 179–192. http://dx.doi.org/10.1111/j.1365-246X.2008.04069.x.

Chan, C.-H., Wu, Y.-M., 2012. A seismicity burst following the 2010M 6.4 Jiashian earthquake – implications for short-term seismic hazards in southern Taiwan. J. Asian Earth Sci. 59, 231–239. http://dx.doi.org/10.1016/j.jseaes.2012.08.011.

Chan, C.-H., Wu, Y.-M., Wang, J.-P., 2012b. Earthquake forecasting using the rate-and-state friction model and a smoothing Kernel: application to Taiwan. Nat. Hazards Earth Syst. Sci. 12 (10), 3045–3057.

Chen, W.-P., Molnar, P., 1977. Seismic moments of major earthquakes and the average rate of slip in central Asia. J. Geophys. Res. 82 (20), 2945–2969. http://dx.doi.org/10.1029/JB082i020p02945.

de la Torre, T.L., Monsalve, G., Sheehan, A.F., Sapkota, S., Wu, F., 2007. Earthquake processes of the Himalayan collision zone in eastern Nepal and the southern Tibetan Plateau. Geophys. J. Int. 171 (2), 718–738. http://dx.doi.org/10.1111/j.1365-246X.2007.03537.x.

Dieterich, J., 1994. A constitutive law for rate of earthquake production and its application to earthquake clustering. J. Geophys. Res. 99 (B2), 2601–2618. http://dx.doi.org/10.1029/93JB02581.

Ekström, G., Nettles, M., Dziewoński, A.M., 2012. The global CMT project 2004–2010: centroid-moment tensors for 13,017 earthquakes. Phys. Earth Planet. Inter. 200–201, 1–9. http://dx.doi.org/10.1016/j.pepi.2012.04.002.

Ellsworth, W.L., Matthews, M.V., Nadeau, R.M., Nishenko, S.P., Reasenberg, P.A., Simpson, R.W., 1999. A physically-based earthquake recurrence model for estimation of long-term earthquake probabilities. Report Rep. 99-522, Reston, VA.

Erdik, M., Demircioglu, M., Sesetyan, K., Durukal, E., Siyahi, B., 2004. Earthquake hazard in Marmara Region, Turkey. Soil Dyn. Earthquake Eng. 24 (8), 605–631. http://dx.doi.org/10.1016/j.soildyn.2004.04.003.

Gansser, A., 1964. Geology of the Himalayas. Interscience Publishers, London, New York.

Goldfinger, C., Nelson, C.H., Morey, A.E., Johnson, J.E., Patton, J.R., Karabanov, E., Gutierrez-Pastor, J., Eriksson, A.T., Gracia, E., Dunhill, G., 2012. Turbidite Event History: Methods and Implications for Holocene Paleoseismicity of the Cascadia Subduction Zone. US Department of the Interior, US Geological Survey.

Green, R.G., Greenfield, T., White, R.S., 2015. Triggered earthquakes suppressed by an evolving stress shadow from a propagating dyke. Nat. Geosci. 8 (8), 629–632. http://dx.doi.org/10.1038/ngeo2491.

Gupta, H.K., Rajendran, K., Singh, H.N., 1986. Seismicity of the North-east India region; Part I, the data base. J. Geol. Soc. India 28 (5), 345–356.

Harris, R.A., 1998. Introduction to special section: stress triggers, stress shadows, and implications for seismic hazard. J. Geophys. Res. 103 (B10), 24347–24358. http://dx.doi.org/10.1029/98jb01576.

Kapp, P., Taylor, M., Stockli, D., Ding, L., 2008. Development of active low-angle normal fault systems during orogenic collapse: insight from Tibet. Geology 36 (1), 7. http://dx.doi.org/10.1130/g24054a.1.

King, G.C., Stein, R.S., Lin, J., 1994. Static stress changes and the triggering of earthquakes. Bull. Seismol. Soc. Am. 84 (3), 935–953.

Lavé, J., Avouac, J.P., 2000. Active folding of fluvial terraces across the Siwaliks Hills, Himalayas of central Nepal. J. Geophys. Res. 105 (B3), 5735–5770. http://dx.doi.org/10.1029/1999jb900292.

Lindsey, E.O., Natsuaki, R., Xu, X., Shimada, M., Hashimoto, M., Melgar, D., Sandwell, D.T., 2015. Line-of-sight displacement from ALOS-2 interferometry: Mw 7.8 Gorkha Earthquake and Mw 7.3 aftershock. Geophys. Res. Lett. 42 (16), 6655–6661. http://dx.doi.org/10.1002/2015GL065385.

Molchan, G.M., 1990. Strategies in strong earthquake prediction. Phys. Earth Planet. Inter. 61 (1–2), 84–98. http://dx.doi.org/10.1016/0031-9201(90)90097-H.

Molchan, G.M., 1991. Earthquake prediction structure of optimal strategies in earthquake prediction. Tectonophysics 193 (4), 267–276. http://dx.doi.org/10.1016/0040-1951(91)90336-Q.

Molina, S., Lindholm, C.D., Bungum, H., 2001. Probabilistic seismic hazard analysis: zoning free versus zoning methodology. Bollettino di Geofisica (selected papers from the 27th ESC, Lisbon, 2000) 42, 19–39.

Mugnier, J.L., Gajurel, A., Huyghe, P., Jayangondaperumal, R., Jouanne, F., Upreti, B., 2013. Structural interpretation of the great earthquakes of the last millennium in the central Himalaya. Earth Sci. Rev. 127, 30–47. http://dx.doi.org/10.1016/j.earscirev.2013.09.003.

Ni, J., Barazangi, M., 1984. Seismotectonics of the Himalayan Collision Zone – geometry of the underthrusting Indian plate beneath the Himalaya. J. Geophys. Res. 89 (B2), 1147–1163. http://dx.doi.org/10.1029/JB089iB02p01147.

Perfettini, H., Avouac, J.P., 2007. Modeling afterslip and aftershocks following the 1992 landers earthquake. J. Geophys. Res.: Solid Earth 112 (B7). http://dx.doi.org/10.1029/2006JB004399, n/a–n/a.

Sapkota, S.N., Bollinger, L., Klinger, Y., Tapponnier, P., Gaudemer, Y., Tiwari, D., 2013. Primary surface ruptures of the great Himalayan earthquakes in 1934 and 1255.

Nat. Geosci. 6 (1), 71–76, http://www.nature.com/ngeo/journal/v6/n1/abs/ngeo1669.html#supplementary-information.

Seeber, L., Armbruster, J.G, 1981. Great detachment earthquakes along the himalayan arc and long-term forecasting. In: Simpson, D.W., Richards, P.G. (Eds.), Earthquake Prediction, An International Review. AGU, Washington, D.C, pp. 259–277, 10.1029/ME004p0259.

Singh, D.D., Gupta, H.K., 1980. Source dynamics of two great earthquakes of the Indian subcontinent: the Bihar-Nepal earthquake of January 15, 1934 and the Quetta earthquake of May 30, 1935. Bull. Seismol. Soc. Am. 70 (3), 757–773.

Toda, S., Stein, R.S., Sevilgen, V., Lin, J., 2011. Coulomb 3.3 Graphic-rich Deformation and Stress-change Software for Earthquake, Tectonic, and Volcano Research and Teaching—User Guide:Rep. Earthquake Science Center, Menlo Park Science Center Menlo Park, California, p. 63.

Uhrhammer, R., 1986. Characteristics of northern and southern California seismicity. Earthquake Notes 57, 21.

Utsu, T., 1961. A statistical study on the occurrence of aftershocks. Geophys. Mag. 30, 521–605.

Weldon, R., Scharer, K., Fumal, T., Biasi, G., 2004. Wrightwood and the earthquake cycle: what a long recurrence record tells us about how faults work. GSA Today 14 (9), 4–10. http://dx.doi.org/10.1130/1052-5173(2004) 014<4: WATECW>2.0CO;2.

Wessel, P., Smith, W.H.F., 1998. New, improved version of generic mapping tools released. Eos, Trans. Am. Geophys. Union 79 (47). http://dx.doi.org/10.1029/98EO000426, 579–579.

Woo, G., 1996. Kernel estimation methods for seismic hazard area source modeling. Bull. Seismol. Soc. Am. 86 (2), 353–362.

Yadav, R.B.S., Bormann, P., Rastogi, B.K., Das, M.C., Chopra, S., 2009. A homogeneous and complete earthquake catalog for northeast India and the adjoining region. Seismol. Res. Lett. 80 (4), 609–627. http://dx.doi.org/10.1785/gssrl.80.4.609.

Zechar, J.D., Gerstenberger, M.C., Rhoades, D.A., 2010. Likelihood-based tests for evaluating space–rate–magnitude earthquake forecasts. Bull. Seismol. Soc. Am. 100 (3), 1184–1195. http://dx.doi.org/10.1785/0120090192.